Available online at www.sciencedirect.com

SCIENCE DIRECT®

International Journal of Heat and Mass Transfer 47 (2004) 4385–4402

International Journal of HEAT and MASS TRANSFER

www.elsevier.com/locate/ijhmt

Numerical investigation of the influence of laser beam mode on melt pool

L. Han, F.W. Liou *

Department of Mechanical and Aerospace Engineering and Engineering Mechanics, University of Missouri, 121 ME Annex, 1870 Miner Circle, Rolla, MO 65409-1060, USA

Received 13 June 2003; received in revised form 15 April 2004

Abstract

During the laser material interaction process, the laser beam mode has significant influence on the formation and development of the melt pool, which directly affects the product quality. In the present study, a mathematical model and related numerical methods have been developed to simulate the process of laser material interaction for different laser beam modes. Three types of symmetric laser beam modes, TEM_{00}, cylindrical TEM_{01}^{*} and TEM_{10} modes, and one nonsymmetrical rectangular TEM_{01} mode are considered. Since spatial distribution of the laser beam intensity varies with beam mode, the formation procedure and the shape of the melt pool in these four cases exhibit quite different features. Flow pattern, which is driven mainly by the thermo-capillary force and recoil pressure, together with temperature distribution are investigated and compared. Physical phenomena such as melting, solidification, vaporization and evolution of the free surface are incorporated in the present model.

Keywords: Laser material interaction; Beam mode; Melt pool; Free surface

1. Introduction

Laser technology has been used in various manufacturing processes to replace conventional manufacturing technologies such as welding, cutting, drilling, cladding, etc. In laser material interaction, laser beam mode plays a critical role in the transport phenomena since the spatial distribution of the laser beam energy varies with the beam mode. In a low laser intensity process, the laser beam mode is primarily responsible for the melt pool shape, flow pattern and temperature distribution, and these factors have a close relationship to the properties of the resulting material structure, such as porosity, microstructure, hardness and surface roughness.

Since the mode selection is an important consideration in the laser manufacturing application, it requires a thorough understanding of the effect of the laser beam mode on the melt pool as well as the nature of the physical phenomena involved. In the past decade, extensive research has been conducted to investigate the laser material interaction process, but most of the work focused on the Gaussian profile laser beam (TEM_{00} mode). There are some models [1–5] which studied the effect of the Gaussian beam mode in the conduction or simplified convection situations due to the complexity of the physical process. Recently, comprehensive models on interaction between the Gaussian laser beam and material in welding applications have been established [6,7]. Those models incorporated the primary phenomena happening in the process, such as melting, solidification and vaporization. Because welding and associated applications need high power density, the Gaussian beam mode is the optimum choice, but in the laser surface treatment, other beam modes such as TEM_{01}^{*} mode may

---

* Corresponding author. Tel.: +1-573-341-4603; fax: +1-573-341-4115.

E-mail address: liou@umr.edu (F.W. Liou).

0017-9310/$ - see front matter © 2004 Published by Elsevier Ltd.
doi:10.1016/j.ijheatmasstransfer.2004.04.036

Nomenclature

A	ambient pressure dependent coefficient
a	laser beam characteristic radius
B_0	evaporation constant
c	specific heat
d	distance in level set function
f	mass fraction
F	speed function in level set evolution equation
g	volume fraction
g_z	gravitational acceleration
h	enthalpy
h_c	convective coefficient
H_ε	Heaviside function
I	laser intensity
L	latent heat fusion
k	thermal conductivity
k_p	equilibrium partition ratio
K	permeability coefficient
$\mathbf{n}$	normal vector
p	pressure
P	laser power
q_{conv}	convection heat loss
q_{evap}	evaporation heat loss
q_{laser}	laser heat flux
q_{radi}	radiation heat loss
S_ϕ	source term in momentum equation
t	simulation time
T	temperature
T_l	liquidus temperature
T_m	melting temperature
T_s	solidus temperature
U	energy of evaporation
u, v, w	velocity components in x-, y- and z-direction
$\mathbf{V}$	velocity vector
V_{dv}	free surface moving speed induced by evaporation
x, y, z	Cartesian coordinate system

Greek symbols

η	laser energy absorptivity coefficient
γ	surface tension coefficient
ε	surface radiation emissivity or transition thickness
κ	free surface curvature
μ_l	dynamic viscosity
σ	Stefan–Boltzmann constant
ρ	density
ϕ	level set function
δ	delta function
λ	volume compensation constant
Ω	computational cell domain

Subscripts

0	initial value or constant
l	liquid phase
s	solid phase
surf	surface cell
v	vapor

Superscripts

m	dimensional index
n	time step number in simulation

offer better advantages [8]. Although the circular laser spot is suitable for most laser applications, there are cases in which a rectangular laser beam mode is preferred [9]. For example, the rectangular TEM$_{01}$ mode has properties similar to dual beam which is used to improve productivity.

A typical schematic view of the laser material process is illustrated in Fig. 1. The laser beam co-axial with a shielding gas nozzle is stationary, and the substrate is positioned below the focal point. In the present study, the Eulerian–Cartesian coordinate system is used and the origin is located on the bottom surface of the substrate and corresponds to the beam center. When the laser beam irradiates the substrate, the surface of the substrate will melt and form the melt pool beneath the laser beam. Fig. 2 gives a high-speed charge coupled device (CCD) camera picture of the melt pool and the adjacent material during the processing [34]. The melt pool was created by a stationary Gaussian beam mode laser with a spot size of 1.0 mm and 1000 W power on the steel substrate.

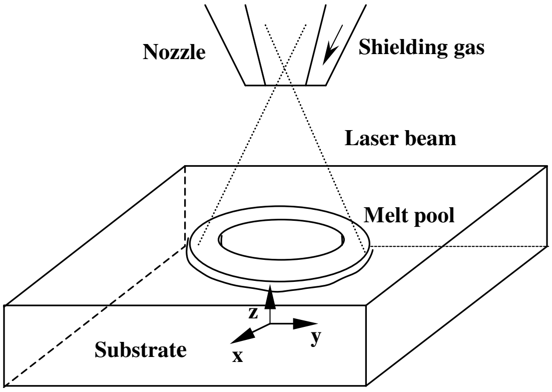

Fig. 1. Schematic diagram of the laser material interaction process.

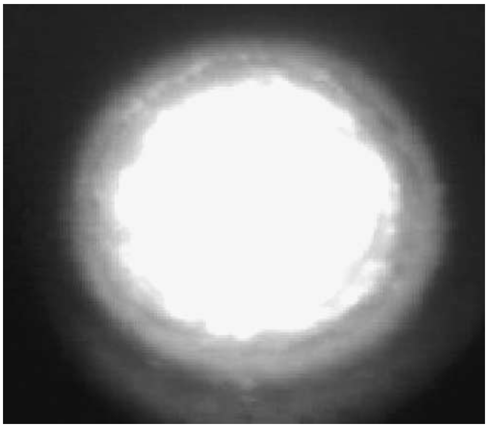

Fig. 2. CCD camera picture of the melt pool and adjacent region during the process.

In this paper, a mathematical model based on the level set algorithm and continuum model is presented. It deals with most phenomena which happen during the laser material interaction, such as melting, solidification, vaporization and free surface evolution phenomena. The continuum model is used to solve Navier–Stokes equations for both solid and liquid regions. Since the level set algorithm can handle the evolution of the free surface, it is incorporated to obtain the solution of the free surface. As the main driving forces, surface tension and thermocapillary force are combined into the model as body forces. The influence of recoil pressure on the deformation of the melt pool has been taken into account in the model.

2. Mathematical model

2.1. Governing equations

A continuum model governing the conservations of mass, momentum and energy has been developed and it may be expressed as seen below:

Mass conservation equation:

$$\frac{\partial}{\partial t}(\rho) + \nabla \cdot (\rho \mathbf{V}) = 0 \tag{1}$$

where the terms for mixture density and mass averaged velocity are defined as follows [13]:

$$\rho = g_s\rho_s + g_l\rho_l \tag{2}$$

$$\mathbf{V} = f_s\mathbf{V}_s + f_l\mathbf{V}_l \tag{3}$$

In the above Eqs. (2) and (3), f_s and f_l refer to mass fractions of solid and liquid, and g_s and g_l are volume fraction of solid and liquid. The relationship of mass fractions and volume fractions satisfies the following equations:

$$f_s = \frac{g_s\rho_s}{\rho} \quad \text{and} \quad f_l = \frac{g_l\rho_l}{\rho} \tag{4}$$

$$f_l + f_s = 1 \quad \text{and} \quad g_s + g_l = 1 \tag{5}$$

Momentum conservation equations:

$$\frac{\partial}{\partial t}(\rho u) + \nabla \cdot (\rho \mathbf{V} u) = \nabla \cdot \left(\mu_l \frac{\rho}{\rho_l}\nabla u\right) - \frac{\partial p}{\partial x} - \frac{\mu_l}{K}\frac{\rho}{\rho_l}(u - u_s) + S_{\phi x} \tag{6}$$

$$\frac{\partial}{\partial t}(\rho v) + \nabla \cdot (\rho \mathbf{V} v) = \nabla \cdot \left(\mu_l \frac{\rho}{\rho_l}\nabla v\right) - \frac{\partial p}{\partial y} - \frac{\mu_l}{K}\frac{\rho}{\rho_l}(v - v_s) + S_{\phi y} \tag{7}$$

$$\frac{\partial}{\partial t}(\rho w) + \nabla \cdot (\rho \mathbf{V} w) = \nabla \cdot \left(\mu_l \frac{\rho}{\rho_l}\nabla w\right) - \frac{\partial p}{\partial z} - \frac{\mu_l}{K}\frac{\rho}{\rho_l}(w - w_s) + \rho g_z + S_{\phi z} \tag{8}$$

In Eqs. (6)–(8), $S_{\phi x}, S_{\phi y}$ and $S_{\phi z}$ are the source terms contributed by surface tension, thermo-capillary force and vapor pressure. Multiplied by the delta function $\delta(\phi)$, those interfacial forces can be treated as body forces and applied to the free surface cells. The delta function $\delta(\phi)$ is the derivative of the mollified Heaviside function which will be discussed in the following section. K is the permeability of the two-phase mushy zone which is modeled as a porous media. Following the approach suggested by Bennon and Incropera [10,11], the present study employs the Kozeny–Carman equation to calculate permeability:

$$K = \frac{K_0 g_l^3}{(1 - g_l)^2} \tag{9}$$

where K_0 is the permeability coefficient.

Energy conservation equation:

$$\frac{\partial(\rho h)}{\partial t} + \nabla \cdot (\rho \mathbf{V} h) = \nabla \cdot \left(\frac{k}{c_s}\nabla h\right) - \nabla \cdot \left(\frac{k}{c_s}\nabla(h_s - h)\right) - \nabla \cdot (\rho(h_l - h)(\mathbf{V} - \mathbf{V}_s)) \tag{10}$$

In Eq. (10) the density, specific heat, thermal conductivity, and the enthalpy are defined as follows [13]:

$$c = f_s c_s + f_l c_l \tag{11}$$

$$k = g_s k_s + g_l k_l \tag{12}$$

$$h = f_s h_s + f_l h_l \tag{13}$$

For implementation purposes, phase specific heats are assumed to be constants, hence the phase enthalpy for the solid and the liquid can be expressed as

$$h_s = \int_0^T c_s \, dT = c_s T \tag{14}$$

$$\begin{aligned} h_l &= \int_0^{T_s} c_s \, dT + L_m + \int_{T_s}^{T} c_l \, dT \\ &= c_l T + (c_s - c_l) T_s + L_m \end{aligned} \tag{15}$$

During the melting and solidification process, the mass fraction of the phase depends on factors such as mixture concentration and the evolution of microstructures. In the present research, based on the level-rule assumption [12] which assumes complete solute diffusion in both the liquid and the solid, phasic concentrations are obtained assuming local thermodynamic equilibrium. For a computational cell whose temperature is between solidus and liquidus temperatures, the thermodynamic relationships are used as the following equation:

$$f_l = 1 - \frac{1}{1 - k_p} \frac{T - T_l}{T - T_m} \tag{16}$$

where k_p is equilibrium partition ratio.

2.2. Tracking of free surface

Several numerical techniques have been developed to solve the evolution of free surface, among which the volume-of-fluid [14,32,33] (VOF) method and the front interface track method [15–17] are two popular ones. Although the front interface track method works well in tracking the evolution of the free surface for the two dimensional cases, it becomes very complicated in the three dimensional situations. The VOF method combined with a continuous surface force [18,19] (CSF) algorithm can solve the evolution of the free surface with surface tension. However, the VOF method is prone to smearing the surface, and an abnormal velocity field near the surface has been reported [20], especially in cases with strong surface shear stress such as laser material interaction. Moreover, in current case, the flow in the melt pool is mainly driven by surface tension, thermo-capillary force and recoil pressure which requires an accurate approach to solve the normal direction and curvature of an irregularly shaped interface. The CSF algorithm computes curvature of the surface by first mollifying the volume fraction using a special method such as B-shape interpolation. The challenge of the CSF method is that if the surface is not smoothed enough, the surface tension may cause the divergence of the velocity field, and if the surface is smoothed too much, the numerical algorithm will not accurately reflect the change in the curvature along the surface.

Recently, the level set method [22–24,30] was developed to track the evolution of the free surface. It does not have the problems mentioned above, since it transforms the interface tracking problem into solving a partial differential equation. The level set method defines a distance function $\phi(\mathbf{x}, t)$ in the domain as follows:

$$\phi(\mathbf{x}, t) = \pm d \tag{17}$$

The interface of the free surface corresponds to zero level set ϕ_0, and the signed distance $\pm d$ represents the actual distance from the zero level set. In this study, level set function ϕ takes $\phi < 0$ in the gas region, and $\phi > 0$ in the solid or liquid region. Hence the function $\phi(\mathbf{x}, t)$ has the following properties:

$$\phi(\mathbf{x}, t) \begin{cases} > 0 & \text{if } \mathbf{x} \in \text{liquid or solid region} \\ = 0 & \text{if } \mathbf{x} \in \Gamma \text{ interface} \\ < 0 & \text{if } \mathbf{x} \in \text{gas region} \end{cases} \tag{18}$$

Level set function evolutes according to the Eq. (19):

$$\frac{\partial \phi}{\partial t} + F|\nabla \phi| = 0 \tag{19}$$

and

$$F = \frac{\partial \mathbf{x}}{\partial t} \cdot \mathbf{n} \tag{20}$$

where F is a speed function evaluated at each point in the domain, and it is a globally defined variable. The speed of F includes propagation expansion speed, curvature dependent speed and normal advection speed.

In this study, narrow band and fast method [22] has been introduced to avoid large computational cost in the interface rebuilding. It can reduce the computational cost from $O(N^m)$ to $O(kN^{m-1})$, here m denotes dimensions, which equals to 3 in this study, and k is the number of the cells in the narrow band.

In order to overcome the numerical difficulties resulting from the properties jump at the interface such as density and viscosity, the assumption is made that the interface has a fixed transition thickness and the physical properties are changing smoothly in the transition area. The mollified Heaviside function has been employed to smooth the properties change. Here the transition thickness is assumed to be 2ε, which corresponds to the width of the narrow band. Mollified Heaviside function has the following formula:

$$H_\varepsilon(\phi) = \begin{cases} 0 & \text{If } \phi < -\varepsilon \\ 0.5\left[1 + \frac{\phi}{\varepsilon} + \frac{1}{\pi}\sin\left(\frac{\pi\phi}{\varepsilon}\right)\right] & \text{If } |\phi| \leqslant \varepsilon \\ 1 & \text{If } \phi > \varepsilon \end{cases} \tag{21}$$

Therefore, the physical properties of the liquid in the transition region can be mollified as

$$\rho_\varepsilon = \rho_1 H_\varepsilon(\phi) + (1 - H_\varepsilon(\phi))\rho_2 \tag{22}$$

$$\mu_\varepsilon = \mu_1 H_\varepsilon(\phi) + (1 - H_\varepsilon(\phi))\mu_2 \tag{23}$$

here, ρ_1 and μ_1 denote properties of liquidus metal, and ρ_2 and μ_2 denote gas properties.

2.3. Boundary conditions

2.3.1. Top free surface

2.3.1.1. Momentum balance on free surface. A free surface cell with one or more gas neighbors is subject to normal and tangential boundary conditions [25] as seen below:

Shear stress balance:

$$\mu\left(\frac{\partial u_s}{\partial n} + \frac{\partial v_n}{\partial s}\right) = \frac{\partial \gamma}{\partial T} \cdot \frac{\partial T}{\partial s} \tag{24}$$

Normal stress balance:

$$p = p_\sigma + p_v \tag{25}$$

where u_s and v_n in Eq. (24) are the tangential and normal velocity components at the free surface. p_σ and p_v appeared in Eq. (25) are the surface tension and the evaporation recoil pressure.

The calculation of surface tension p_σ is given by

$$p_\sigma = \gamma \cdot \kappa \tag{26}$$

here γ and κ represent surface tension coefficient and curvature respectively. In the present study, the surface tension with temperature $\partial\gamma/\partial T$ is assumed to be a constant. The unit normal on the interface, drawn from the gas into the liquid or solid, and the curvature of the interface can be expressed in terms of $\phi(\mathbf{x}, t)$:

$$\mathbf{n} = \left.\frac{\nabla\phi}{|\nabla\phi|}\right|_{\phi=0} \tag{27}$$

and

$$\kappa = \nabla \cdot \left.\left(\frac{\nabla\phi}{|\nabla\phi|}\right)\right|_{\phi=0} \tag{28}$$

Recoil vapor pressure [26] applied to the free surface according to the following equation:

$$p_v = AB_0\sqrt{T_{\text{surf}}}\exp\left(\frac{-U}{T_{\text{surf}}}\right) \tag{29}$$

where A is an ambient pressure dependent coefficient, B_0 is the evaporation constant, T_{surf} is the surface cell temperature, and U is energy of evaporation.

2.3.1.2. Energy balance on free surface. Energy balance on free surface satisfies the following equation:

$$k\frac{\partial T}{\partial \mathbf{n}} = q_{\text{laser}} - q_{\text{radi}} - q_{\text{conv}} - q_{\text{evap}} \tag{30}$$

where q_{conv}, q_{radi} and q_{evap} refer to convection heat loss, radiation emission heat loss and evaporation heat loss, respectively. The amount of those terms can be obtained using the following formulas

$$q_{\text{conv}} = h_c(T - T_\infty) \tag{31}$$

$$q_{\text{rad}} = \varepsilon\sigma(T^4 - T_\infty^4) \tag{32}$$

$$q_{\text{evap}} = \rho V_{\text{dv}} L_v \tag{33}$$

In the above Eqs. (31)–(33), h_c is convective coefficient, ε is radiation coefficient, σ is Stefan–Boltzmann constant, T_∞ is ambient temperature, L_v is the latent heat of evaporation, V_{dv} is the component of the boundary velocity contributed by the evaporation, which can be expressed by Eq. (34):

$$V_{\text{dv}} = V_0 \exp\left(-\frac{U}{T_{\text{surf}}}\right) \tag{34}$$

where V_0 is the order of magnitude of the sound velocity in the material.

The heat losses induced by convection, radiation and evaporation are a function of the surface temperature and increase with the rising of the surface temperature. As the surface temperature is heated up to over 3000 K, the heat loss is dominated by evaporation, and it is nearly comparable to the laser heat influx in current study cases.

On the free surface, incoming energy from the laser irradiation is given by

$$q_{\text{laser}}(x, y) = \eta I(x, y)\delta(\phi) \tag{35}$$

where $I(x, y)$ is the intensity of the laser beam at the location of (x, y). The delta function $\delta(\phi)$ is used to guarantee the laser irradiation only acts on the surface. η is the absorption coefficient, which depends on the material property of the substrate, temperature and surface roughness. In this study, absorption coefficient η is assumed to be constant throughout the process.

Intensity distribution for the TEM_{00}, cylindrical TEM_{01}^* and TEM_{10} modes as well as rectangular TEM_{01} mode have the following formulas respectively:

$$\text{TEM}_{00} : I(x, y) = \frac{2P}{\pi a^2}\exp\left[-\frac{2(x^2 + y^2)}{a^2}\right] \tag{36}$$

$$\text{TEM}_{01}^* : I(x, y) = \frac{4P}{\pi a^2} \cdot \frac{(x^2 + y^2)}{a^2}\exp\left[-\frac{2(x^2 + y^2)}{a^2}\right] \tag{37}$$

$$\text{TEM}_{10} : I(x, y) = \frac{2P}{\pi a^2}\left[1 - \frac{2(x^2 + y^2)}{a^2}\right]^2 \exp\left[-\frac{2(x^2 + y^2)}{a^2}\right] \tag{38}$$

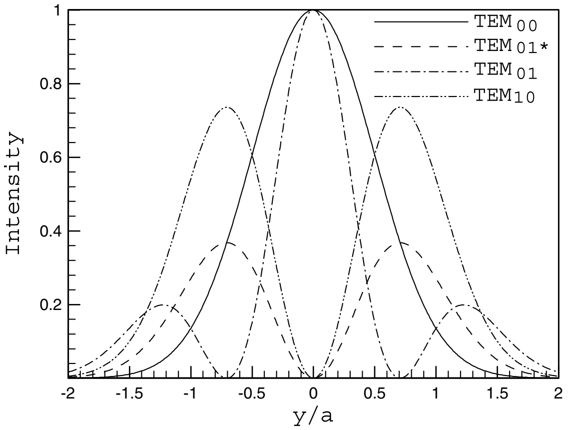

Fig. 3. Intensity distribution of four different laser beam modes along *y*-axis.

$$\mathrm{TEM}_{01}: I(x,y) = \frac{8P}{\pi a^2}\cdot\frac{y^2}{a^2}\exp\left[-\frac{2(x^2+y^2)}{a^2}\right] \tag{39}$$

here it is assumed that the beam shape does not change along the propagation direction. The intensity profile curves are illustrated in Fig. 3. For the rectangular TEM_{01} mode, it is not symmetric, and the curve shows the intensity distribution along the *y*-axis.

2.3.2. Bottom and side surfaces

$$-k\frac{\partial T}{\partial \mathbf{n}} = h_c(T - T_\infty) \tag{40}$$

$$u = 0, \quad v = 0, \quad \text{and} \quad w = 0 \tag{41}$$

3. Numerical considerations

Since the energy equation implicitly contains the phase change effect and the momentum equations introduce the damping terms, the governing equations of mass, momentum and energy conservation are applicable for both solid and liquid phases. A semi-implicit finite difference algorithm has been used for the solution of continuity and momentum equations. The thermal energy transport equation is solved using an explicit finite volume approximation method [21].

3.1. Steps of iteration procedure

1. Initialize the computational variables ϕ, u, v, w, T and p. Let level set function ϕ be the signed normal distance to surface, and set divergence-free velocity (identically zero in the study), room temperature and relative atmosphere reference pressure as initial values for u, v, w, T and p.
2. Solve the momentum equations using the projection method [27,28]. First, calculate the source term including surface tension, thermo-capillary force and vapor pressure. Then substitute them into the momentum equations to calculate the velocities. Subsequently, project the velocities to be divergence-free to solve the pressure, hence, obtain the new time velocities. See below for details about the projection method.
3. Advance the level set function in time using the 3rd order essential non-oscillation (ENO) [29] method, and update the free surface to its new location $\phi^{n+1/2}$.
4. Reinitialize the level set function $\phi^{n+1/2}$ by solving the following equation to a steady state with an initial level set value $\phi(\mathbf{x},0) = \phi^{n+1/2}$:
$$\phi_\tau = S_\varepsilon(\phi^{n+1/2})(1 - |\nabla\phi|) \tag{42}$$
where S_ε is a smooth factor and τ is artificial time. Denotes the solution by ϕ^{n+1}.
5. Solve the energy equation using the newly obtained values in steps 2–4.
6. Replace old velocities, pressure, temperature and level set function by new values, and return to step 2 for the next iteration until the time to finish is reached.

3.2. Projection method

The projection method is used to solve the velocity and pressure and could be described below:

First, rewrite the momentum equation as seen below:

$$\mathbf{V}_t + \frac{1}{\rho^n}\nabla p^{n+1} = \mathbf{V}^*(\mathbf{V}^n, \phi^n) \tag{43}$$

Then, taking the divergence of both sides of the Eq. (43), and using the fact that $\nabla\cdot\mathbf{V}_t = 0$ to reduce the momentum equation to the following form for pressure:

$$\nabla\cdot\frac{1}{\rho^n}\nabla p^{n+1} = \nabla\cdot\mathbf{V}^*(\mathbf{V}^n, \phi^n) \tag{44}$$

Eq. (44) is the pressure Poisson equation, and it can be solved by the successive over relaxation (SOR) method or the conjugate-gradient (CG) method.

After solving Eq. (44) for ∇p, update the value for $\mathbf{V}_t$ by

$$\mathbf{V}_t = \mathbf{V}^*(\mathbf{V}^n, \phi^n) - \frac{1}{\rho^n}\nabla p^{n+1} \tag{45}$$

Therefore, if defining the projection operator $\mathbf{P}$ as

$$\mathbf{V}_t = \mathbf{P}(\mathbf{V}^*) \tag{46}$$

Eq. (45) can be expressed as

$$\frac{1}{\rho}\nabla p = \mathbf{V}^{*} - \mathbf{V}_{t} = \mathbf{V}^{*} - \mathbf{P}(\mathbf{V}^{*}) = (\mathbf{I} - \mathbf{P})(\mathbf{V}^{*}) \tag{47}$$

3.3. Volume conservation algorithm

It is essential to maintain the level set function as the signed distance from the interface all the time. In the numerical implementation, it was observed that the reinitialization operation changed the zero level set ϕ_0 and it caused the partial volume loss of the surface cell. Based on the work of Sussman et al. [31], the following constraint was placed in each computational cell Ω:

$$\frac{\partial V}{\partial \tau} = \frac{\partial}{\partial \tau}\int_{\Omega} H(\phi)\,\mathrm{d}\Omega = 0 \tag{48}$$

The Eq. (48) can be rewritten as

$$\int_{\Omega} H'(\phi)\phi_{\tau}\,\mathrm{d}\Omega = 0 \tag{49}$$

In order to compensate the volume loss, reinitialization Eq. (42) is modified as

$$\phi_{\tau} = S_{\varepsilon}(\phi)(1 + |\nabla\phi|) + \lambda \cdot f(\phi) \tag{50}$$

where λ is a constant in each cell, and function $f(\phi)$ has the form:

$$f(\phi) \equiv H'(\phi)|\nabla\phi| \tag{51}$$

Denote $L(\phi_0, \phi)$ as

$$L(\phi_0, \phi) = S_{\varepsilon}(\phi_0)(1 + |\nabla\phi|) \tag{52}$$

Combined Eqs. (49) through (52), λ can be solved as

$$\lambda = \frac{-\int_{\Omega} H'(\phi)L(\phi_0, \phi)\,\mathrm{d}\Omega}{\int_{\Omega} H'(\phi)f(\phi)\,\mathrm{d}\Omega} \tag{53}$$

Once obtaining the value of λ, the compensation amount for ϕ can be calculated through Eq. (50). After placing volume constraint on each computational cell, the amount of total mass loss is less than 1% in the current study cases. In order to accurately track the evolution of the melt pool, a small mesh size as much as 0.03 mm was used and the time step was set to be 10^{-5} s to satisfy convergence condition.

4. Results and discussions

In this study, the same process parameters are utilized in all four cases. The laser beam has a power of 1000 W and a characteristic diameter of 500 μm. Stainless steel 304 is selected as the substrate material and a 0.2 absorptivity coefficient is assumed. Thermal properties of stainless steel 304 are listed in Table 1. The simulation of the process starts when the laser beam is turned on and ends when the melt pool approaches a

Table 1
Material properties of the steel and simulation conditions

Property	Symbol	Value (unit)
Solid specific heat	c_{s}	460 J/kg K
Liquid specific heat	c_{l}	480 J/kg K
Solid thermal conductivity	k_{s}	21 W/m K
Liquid thermal conductivity	k_{l}	21 W/m K
Solid density	ρ_{s}	7500 kg/m^3
Liquid density	ρ_{l}	6900 kg/m^3
Latent heat of fusion	L_{m}	2.5×10^{5} J/kg
Latent heat of evaporation	L_{v}	6.0×10^{6} J/kg
Melting temperature	T_{m}	1730 K
Boiling temperature	T_{v}	3400 K
Permeability coefficient	K_0	5.0×10^{-11}
Equilibrium partition ratio	k_{p}	0.3
Laser absorptivity	η	0.2
Dynamic viscosity	μ_{l}	6.0×10^{-3} kg/ms
Radiation emissivity	ε	0.3
Convective coefficient	h_{c}	10 W/m^2 K
Laser power	P	1000 W
Laser beam characteristic diameter	a	5.0×10^{-4} m
Surface tension with temperature	$\partial\gamma/\partial T$	-4.3×10^{-4} N/m K
Surface tension at melting point	γ	1.9 N/m
Atmosphere pressure	P_{∞}	1.013×10^{5} Pa
Ambient temperature	T_{∞}	300 K
Stefan–Boltzmann's constant	σ	5.67×10^{-8} W/m^2 K^4
Vaporization constant	B_0	1.78×10^{10} Pa
Ambient pressure coefficient	A	0.55

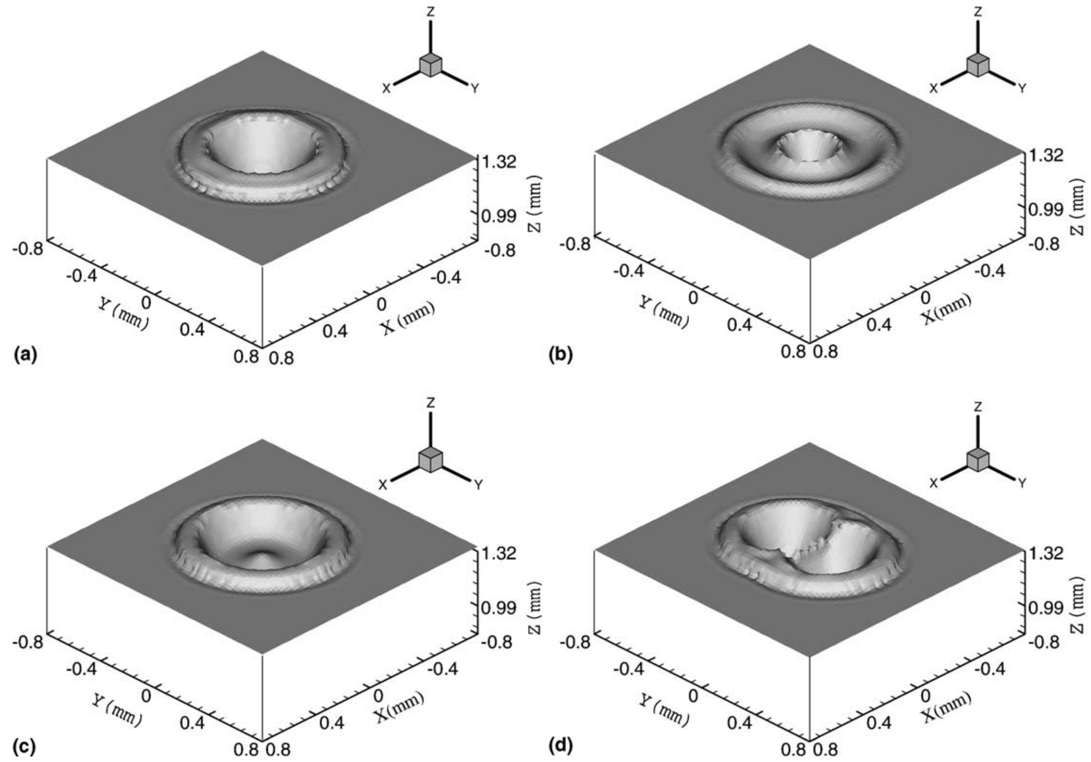

Fig. 4. Partial 3D view of the melt pool shape at $t = 12$ ms. (a) TEM_{00}, (b) TEM_{10}, (c) TEM_{01}^{*}, and (d) TEM_{01}.

stable state. As the laser beam irradiates on the surface of the substrate, the region under the laser beam is melted to form the melt pool, which is surrounded by the solid part. Fig. 4 illustrates the surface deformation of four different types of laser beam modes at simulation time $t = 12$ ms. Formation and evolution of the melt pool vary with different laser beam modes. Several representative stages during the evolution period are presented to show the differences in the formation and development of the melt pool for different laser beam modes, and the lapse time between every two consecutive plots may not be equal. Detailed mechanisms of the melt pool formation will be discussed below.

4.1. *Influences of the beam mode on the formation and evolution of melt pool*

4.1.1. *TEM$_{00}$ mode*

The intensity profile of the TEM_{00} mode satisfies the Gaussian distribution, and reaches a peak value of $I_0 = \frac{2P}{\pi a^2}$ at the beam center. When the thermal flux enters the substrate, the melt pool first appears beneath the beam center, and expands to the whole beam spot in less than 4 ms, as seen in Fig. 5(a). Due to the presence of the huge temperature gradient, which causes the strong Marangoni shear stress, the molten surface fluid at the melt pool center is driven outwards. The outward flowing fluid with a high temperature assists the heat to dissipate in the radial direction, and it partially extends the melt pool diameter. When the surface liquid is pulled away from the center of the melt pool, the surface is depressed in the central region and a crater is formed there. The displaced fluid builds up around the shoulder of the melt pool and causes the surface to bulge upward, and then it is dragged down to the solid surface of the substrate along the radial direction by the gravity force, wall adhesion and surface tension.

It can be noted from the velocity field in Fig. 5(a) that, in the beginning stage, the melt pool is shallower and the liquid layer is very thin. As the liquid layer thickness increases, there is a separation observed in the fluid flow. The bottom part of the liquid layer has a slow velocity initially and is accelerated due to the viscous shear stress from the much faster surface flow. When the bottom fluid from the center region reaches the S/L boundary, it turns down and circulates back to the central region, which leads to the formation of the vortex near the shoulder. A weak vortex can be seen in Fig. 5(a) at $t = 12$ ms, and it is strengthened gradually until almost all of the displaced fluid recirculates back. Meanwhile, the diameter and depth of the crater are expanded as well while the melt pool becomes wider and

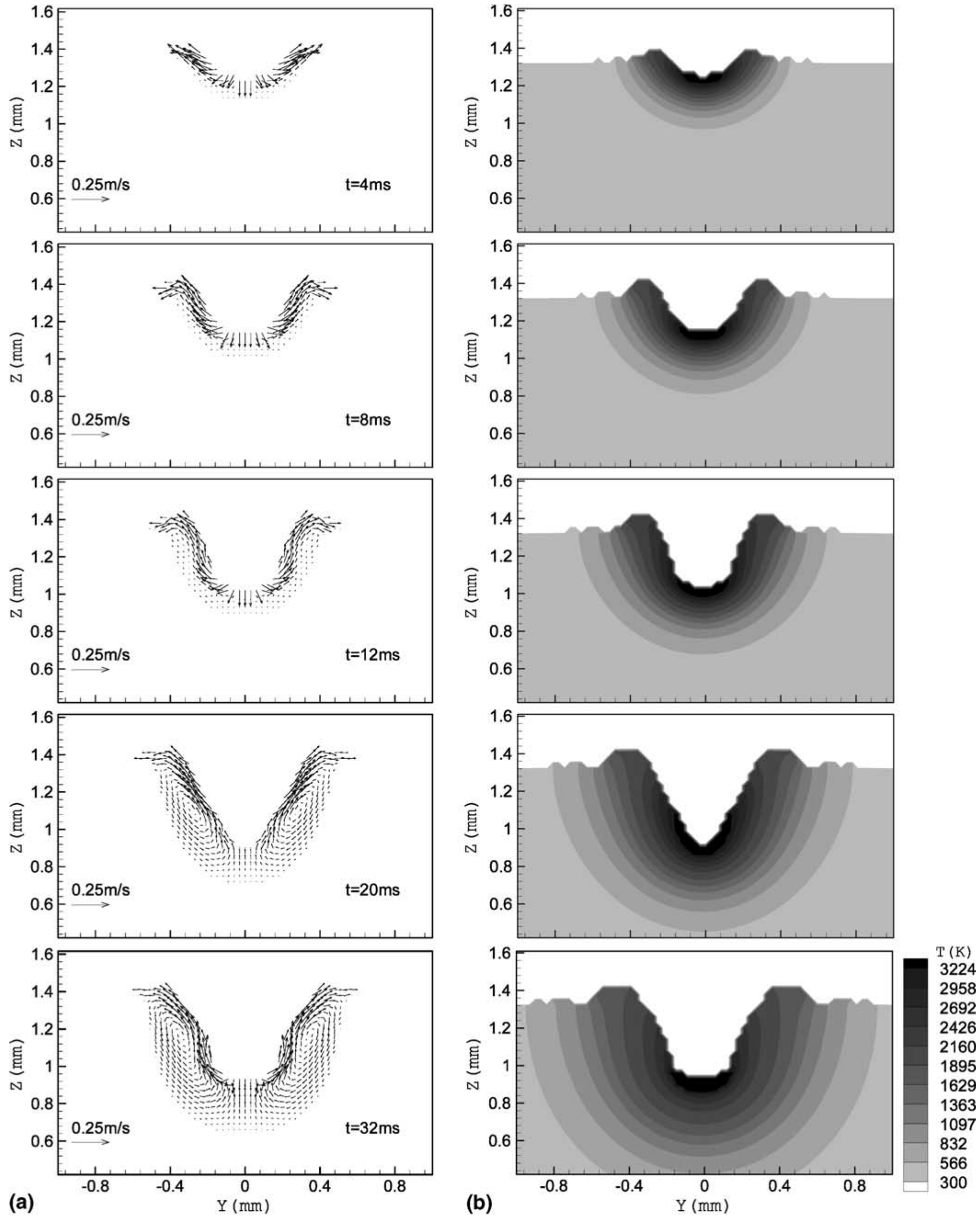

Fig. 5. Evolution of the melt pool for TEM_{00} mode. (a) Velocity field and (b) temperature field.

deeper. In addition, due to the high intensity energy concentrating on the central region, strong evaporation takes place there, and evaporation recoil pressure attributes to the further depression of the surface.

4.1.2. Cylindrical TEM_{01}^{*} mode

Fig. 6(a) and (b) show the evolution of velocity field and temperature distribution of the melt pool for the cylindrical TEM_{01}^{*} mode. Corresponding to the intensity distribution which concentrates in a ring band area located around $r = \frac{\sqrt{2}}{2}a$ with a peak intensity of $I \approx \frac{0.736P}{\pi a^2}$, the melt pool initiates at the ring band region and the molten surface fluid is driven away from the band region by the Marangoni shear stress, which exists both inward and outward in the radial direction. Under the effects of the heat conduction and convection from the surrounding region, the material in the central region was melted. The inward surface flow squeezes the molten

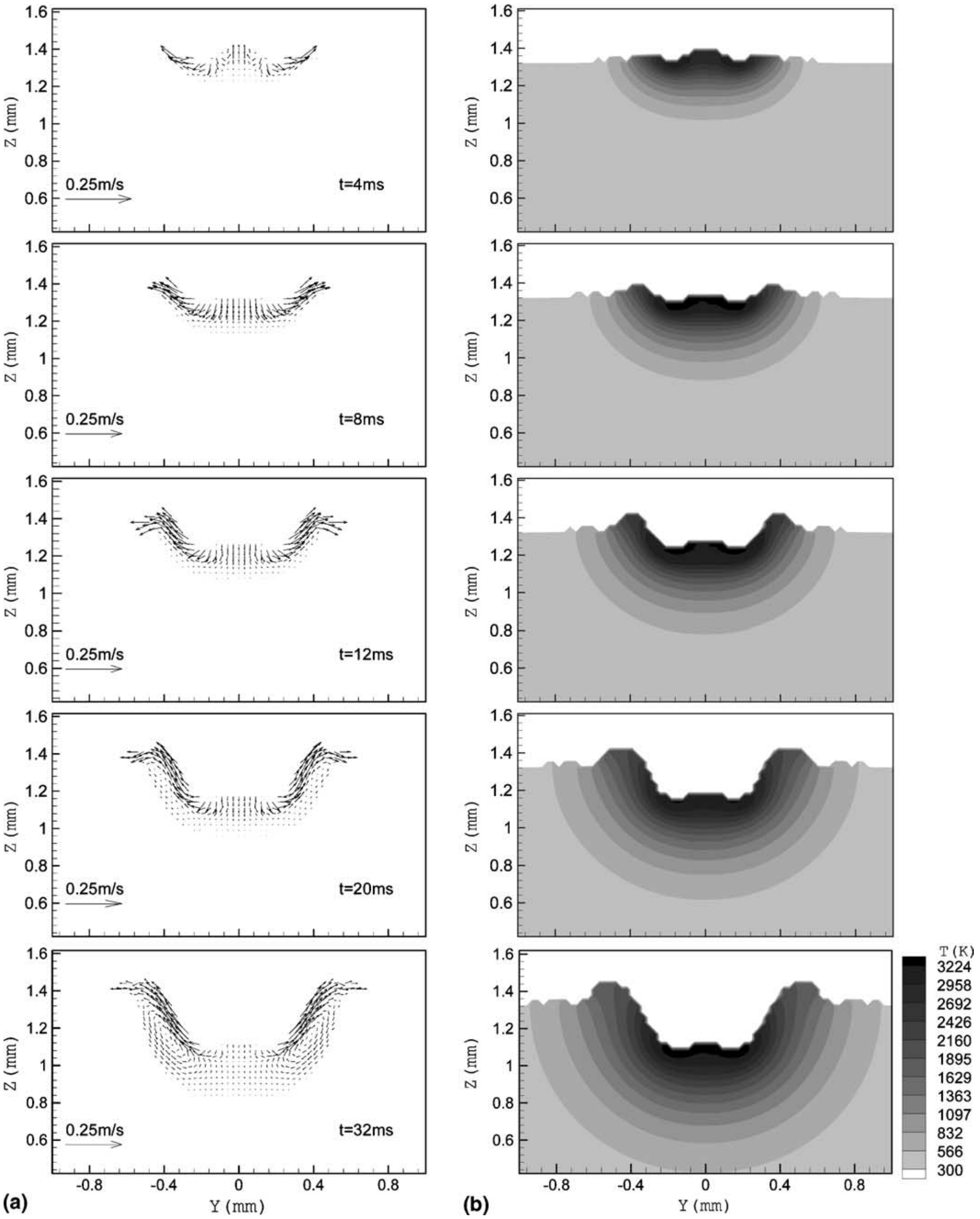

Fig. 6. Evolution of the melt pool for cylindrical TEM_{01}^{*} mode. (a) Velocity field and (b) temperature field.

fluid upward, which causes the surface of the central part to be slightly higher than the other regions as shown $t = 4$ ms in Fig. 6. After a certain time, the surface of the central part starts to drop. This procedure can be identified through changes of velocity fields from $t = 4$ to 8 ms. In the meantime, fluid flow in the central region has undergone a transition from upward to downward due to the surface tension and vapor pressure exceeding the upward Marangoni shear stress.

Subsequently, the surface fluid which is brought away by the outward flow in the ring band region, is compensated by the displaced fluid from the central region and the melt pool surface in the central region falls down further. At the same time, the shoulder becomes higher and wider until the vortex is generated by a mechanism similar to the TEM_{00} mode. Contrary to the TEM_{00} mode, the deepest depressed part of the surface is a circular zone, instead of the position underneath the beam center. Since the energy is distributed across a broader area and the peak intensity is approximately 40% as much as in the TEM_{00} mode, the melt pool shape looks like a basin and has less penetration features. The temperature distribution plots indicate that, in the early stage of the melt pool development, isotherms in the liquid region have a wave shape, which is consistent with the intensity profile. After the melt pool is developed, temperature difference between the central part and the surrounding part has been diminished, and the isotherms tend to be smoother.

4.1.3. Rectangular TEM_{01} mode

Melt pool variation of the rectangular TEM_{01} mode has the features of the dual Gaussian laser beam. Initially, two hot spots occur corresponding to the

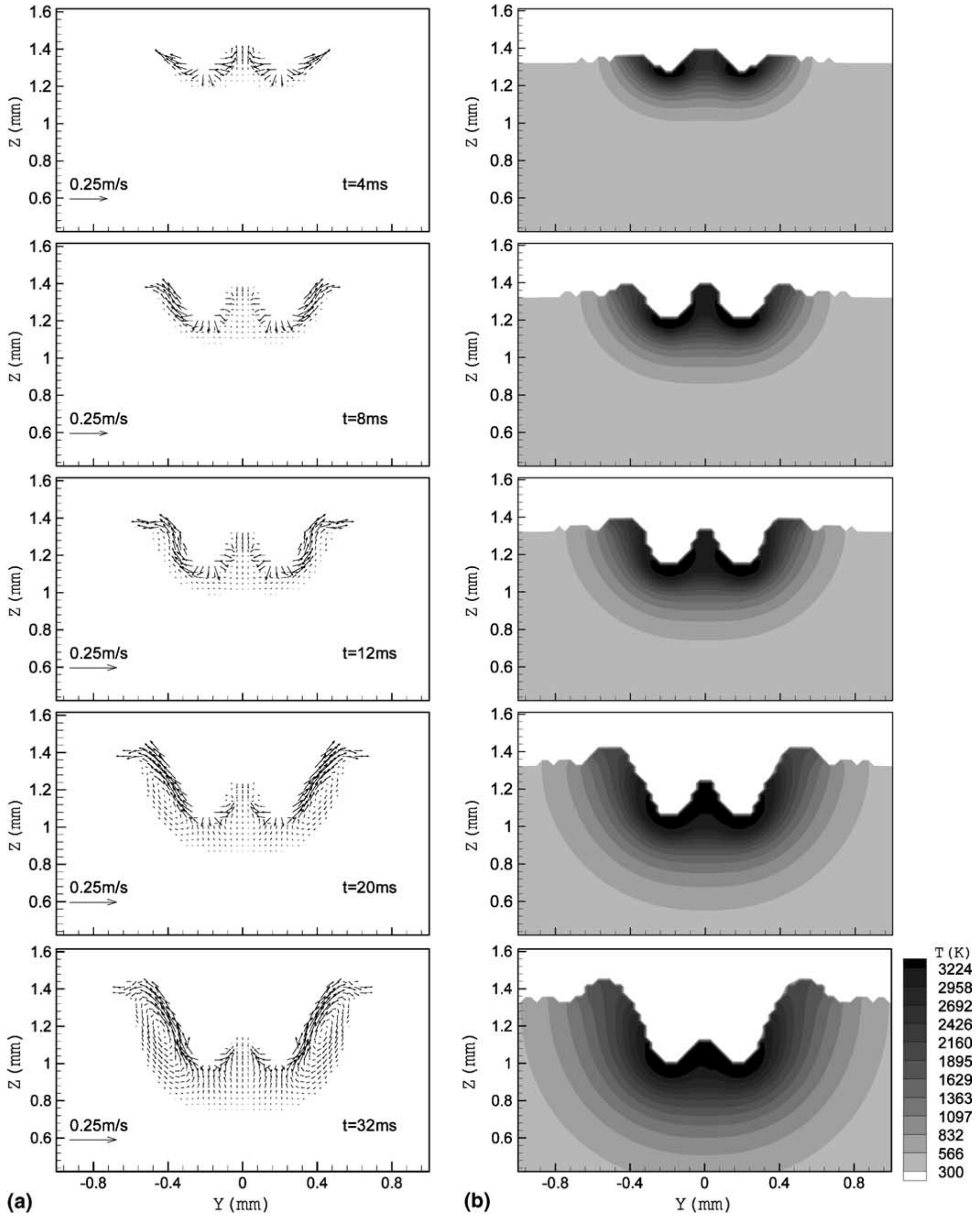

Fig. 7. Evolution of the melt pool for rectangular TEM_{01} mode along y-axis. (a) Velocity field and (b) temperature field.

locations of the intensity peaks and they develop to be the two separate melt pools as more heat flux transports into the substrate. These two melt pools enlarge further until they join together, as seen in Fig. 7. Since higher beam intensity is reached in the area irradiated by the laser beam in comparison to the cylindrical TEM_{01}^{*} mode, the melt pool and the crater are deeper and smaller in the rectangular TEM_{01} mode. After two separate melt pools unite together, in the y-direction, surface fluid in the central region has a lower temperature than the surrounding region, which leads the surface fluid to flow towards the center. At the same time, in the x-direction its temperature is still higher than the nearby region, as a result, the incoming fluid from y-direction is dragged to x-direction, and then circulates back to the bottom of the melt pool as shown in Figs. 7(a) and 8(a). This specific flow pattern distinguishes it from the TEM_{01}^{*} mode. Additionally, zero intensity property on the x-axis causes the presence of the dam-shaped liquid zone, which separates the craters and has a tendency to collapse throughout the melt pool development. Isotherms appear to be quite different in $x = 0$ plane and $y = 0$ plane after the melt pool is formed due to the nonsymmetrical intensity distribution. Figs. 7(b) and 8(b) present the temperature distributions of the cross-section through y- and x-axis at $t = 32$ ms. In the $x = 0$ plane, isotherms are concave in the central region, and fluctuate in the liquid region. In contrast, isotherms in $y = 0$ plane are smoother and more regular.

4.1.4. Cylindrical TEM_{10} mode

The cylindrical TEM_{10} mode can be treated as the superposition of cylindrical TEM_{00} and TEM_{01}^{*} modes, and the laser material interaction zone consists of two parts: one is the central circular region, where the intensity profile is similar to the TEM_{00} mode with the same peak intensity, but the area is smaller; the other is the ring band region surrounding the central part, where the intensity has a profile similar to the cylindrical TEM_{01}^{*} mode, but peak intensity is approximately 50% lower. Hence, the formation and evolution of the melt pool exhibit the characteristics of both TEM_{00} and TEM_{01}^{*} modes.

From Fig. 9(a) and (b), it can been seen that high intensity energy at the beam center heats the substrate surface up to a melting temperature in a very short time. Subsequently, the substrate in the ring band region starts to melt as well. Corresponding to a substantial intensity variation, there is a higher temperature gradient in the central region than in the TEM_{00} mode, which causes the molten surface there to depress deeper and narrower. The molten fluid in the central circular region is pulled away by the strong Marangoni shear stress and flows outward to the ring band region. The flow from the central region has a greater magnitude of radial velocity than that in the band region, and causes the fluid there downward to generate a circular ripple as seen in Fig. 4(b). The ripple facilitates the formation of the vortex, and a strong vortex has occurred at $t = 12$ ms, which is earlier than the other three laser beam modes. The flow bifurcates at the valley of the ripple. Partial surface fluid turns downward and circulates back to the center, and the rest continues to flow outward. The outflow fluid generates another vortex near the shoulder in the same manner as the TEM_{00} mode. Before the second vortex is fully developed, part of the displaced fluid from the melt pool center joins the circulation of the second vortex; thereby, the surface in the central region sinks further, as illustrated in Fig. 9(a) from $t = 12$ to 32 ms. Inside the melt pool, the flow pattern considerably affects the isotherms and the melt pool shape. As compared to the other three modes, the complicated flow pattern causes isotherms in the liquid region to be more irregular.

4.2. Top view of the melt pool

Fig. 10 illustrates the velocity field from the top view at $t = 32$ ms, when the melt pools in all four cases are close to fully developed states. Cross-reference to Figs. 5 through 9 is helpful to visualize the velocity field. In the symmetric beam mode TEM_{00}, TEM_{01}^{*} and TEM_{10}, the common feature of the velocity field is that surface fluid

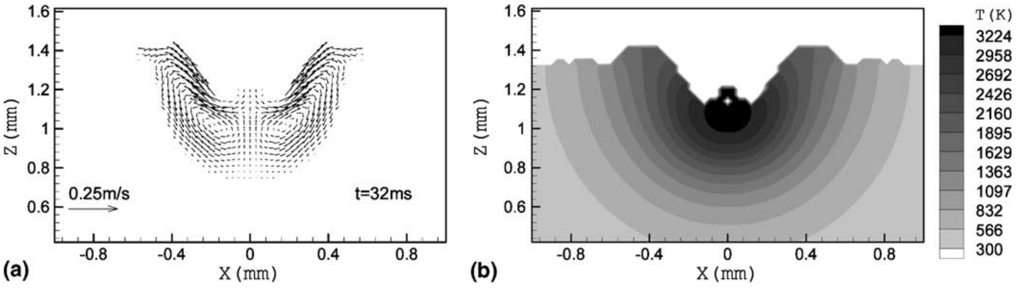

Fig. 8. Melt pool for rectangular TEM_{01} mode along x-axis at $t = 32$ ms. (a) Velocity field and (b) temperature field.

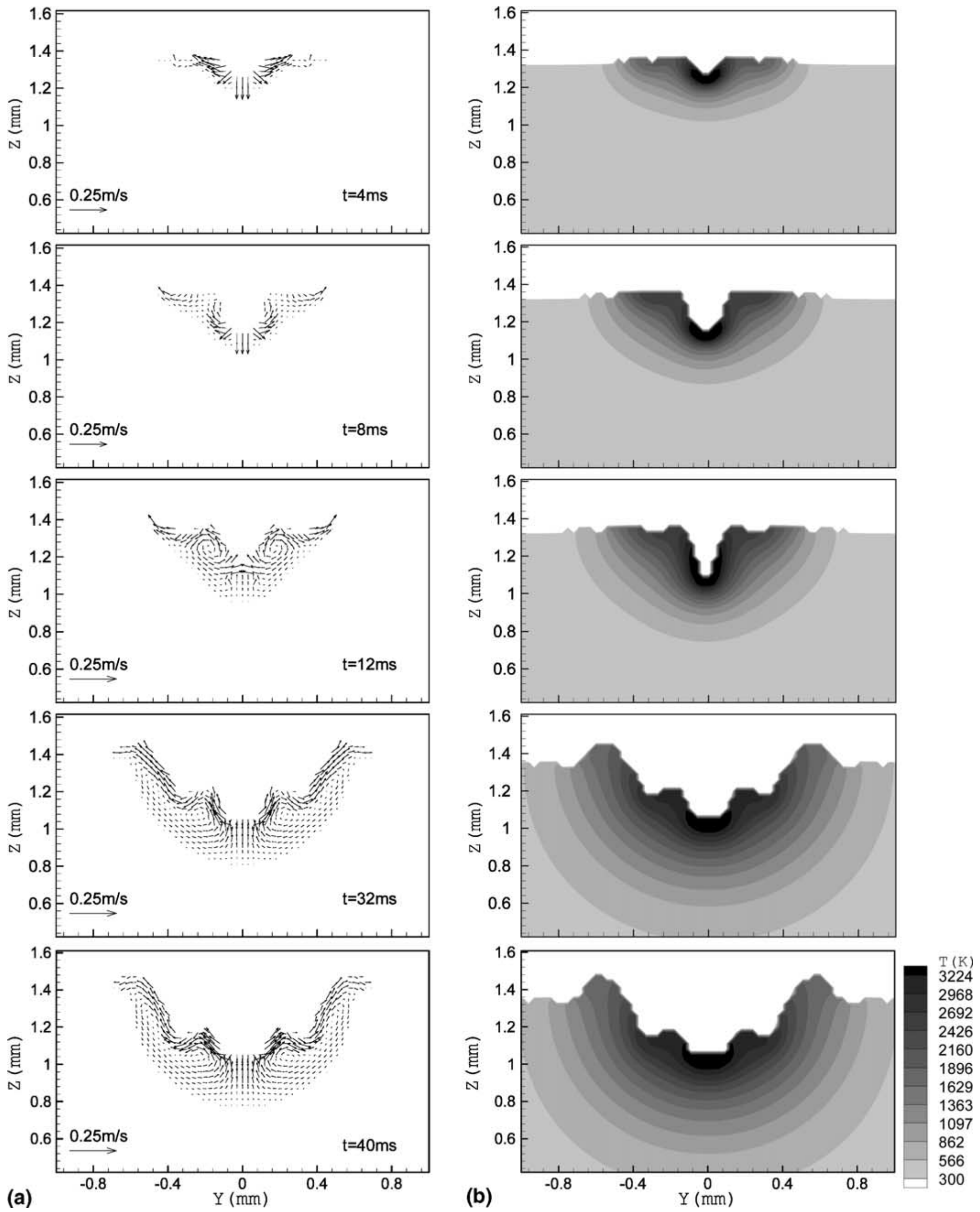

Fig. 9. Evolution of the melt pool for cylindrical TEM_{10} mode. (a) Velocity field and (b) temperature field.

flows outward from the melt pool center to the edge, however, the magnitudes of the velocity are quite different. For the rectangular TEM_{01} mode, the fluids from two hot spot zones collide in the melt pool center and make a turn to the x-direction, and then the surface fluid flows to the edge of the melt pool in the direction parallel to the x-axis.

The surface temperature distribution corresponds to the above velocity field as shown in Fig. 11. Surface temperature is a function of the beam intensity profile; however, flow pattern also plays a significant role in the temperature distribution. As seen in the plots, maximum surface temperature points may not agree well with the peak intensity locations. For cylindrical TEM^*_{01} mode and rectangular TEM_{01} mode, the maximum surface temperature locations shift slightly toward the beam center partially induced by the strong surface flow.

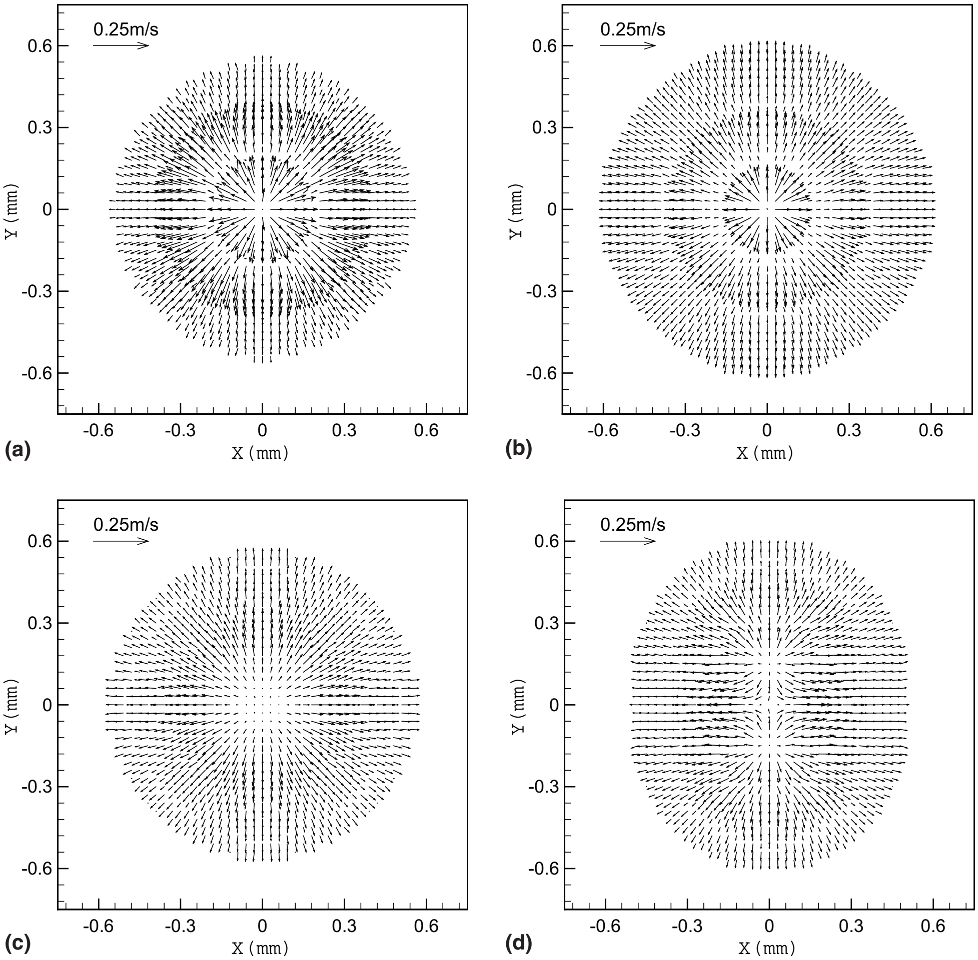

Fig. 10. Velocity field from the top view. (a) TEM_{00}, (b) TEM_{10}, (c) TEM^*_{01}, and (d) TEM_{01}.

4.3. Effect of recoil vapor pressure on melt pool shape

The effect of the recoil vapor pressure on melt pool shape is examined by conducting the simulations with and without considering the recoil vapor pressure. Fig. 12 presents the locations of the melt pool surface and solid/liquid interface at $t = 36$ ms. The deformation of the melt pool surface and the formation of the crater are primarily contributed by the Marangoni effect in all four cases. However, at the high beam intensity region where the surface temperature is more than 3000 K, the melt pool surface is affected considerably by the recoil vapor pressure in all four cases as shown in Fig. 12. The strong vapor pressure plays apparent roles in two aspects: on the one hand, the surface fluid in high temperature is pushed to the outside and expands the melt pool diameter in a mechanism similar to the Marangoni effect; on the other hand, deeper surface depression facilitates the heat to dissipate in the depth direction and increases the melt pool penetration, which can be identified through the change of the solid/liquid interfaces.

4.4. Melt pool aspect ratio analysis

Aspect ratio refers to the ratio of the melt pool depth to the diameter. For the non-symmetric TEM_{01} mode, the melt pool width on $x = 0$ plane is used as the diameter in the following analysis. The laser beam peak intensity and the area of high laser intensity interaction zone are two critical factors affecting the time to melt the substrate, and corresponding times for cylindrical TEM_{00}, TEM^*_{01} and TEM_{10} modes and rectangular TEM_{01} mode are 0.128, 0.9, 0.208 and 0.152 ms, respectively. The variations of the depth, diameter and aspect ratio with the time for these four beam modes are presented in Fig. 13(a), (b) and (c). The general trend is that, at the formation stage ($t < 30$ ms), the depth and diameter of the melt pool extend rapidly, and then the

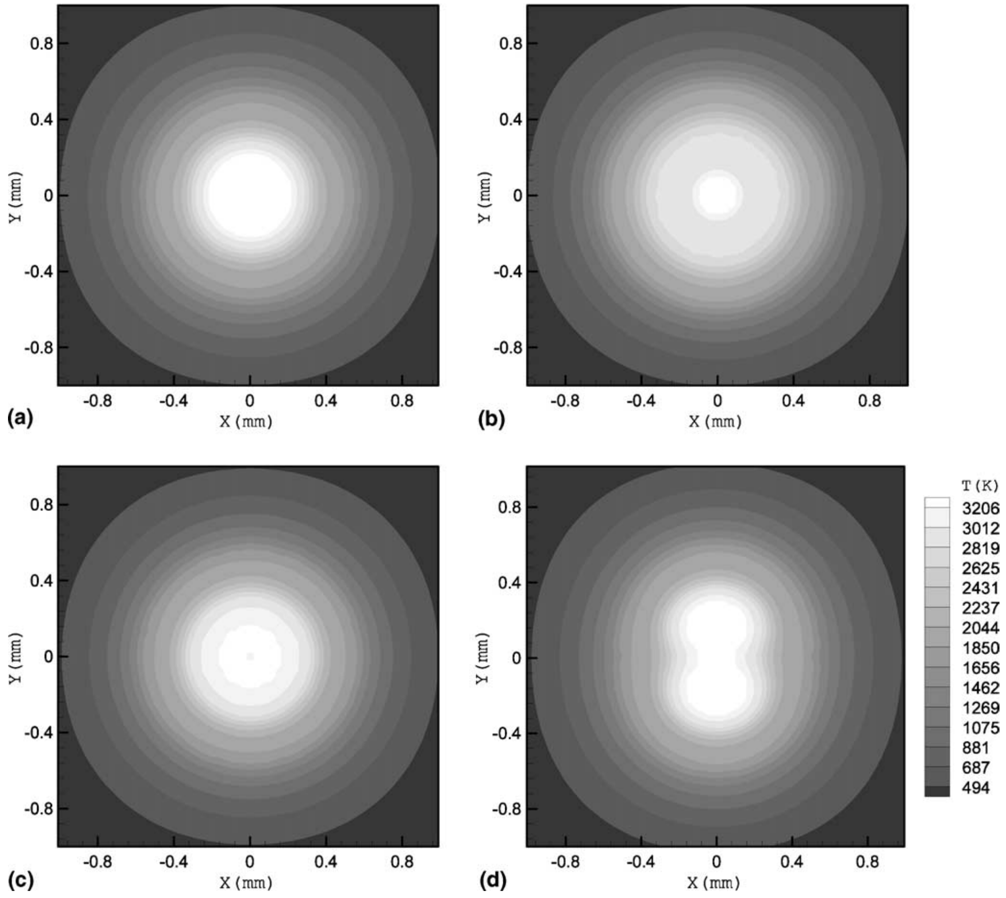

Fig. 11. Temperature field from the top view. (a) TEM_{00}, (b) TEM_{10}, (c) TEM^{*}_{01}, and (d) TEM_{01}.

expansion speed slows down; ultimately, the melt pool size approaches to a stable state. At that point, all the energy from the laser beam sinks into the substrate and dissipates into the ambient through evaporation, radiation and convection. In comparison to the depth evolution, the melt pool diameter develops more quickly at the beginning stage. As shown in Fig. 13(b), at time about 4ms, melt pool diameters have reached more than 0.6 mm, which is over half of the size at the stable state, while it takes more than 10 ms to reach a half depth of stable state. In all four cases at the fully developed stage, although conduction accounts for more than 90% heat dissipation in the melt pool region, the influence of the convection on the aspect ratio cannot be neglected since the melt pool deformation arising from convection exerts essential effects on the melt pool shape.

However, there are significant differences for the variation of the aspect ratio among the four types of beam modes. As seen in Fig. 13(a) and (b), the melt pool in the case of the TEM_{00} mode is deeper and smaller than the other three beam modes after 4 ms, since at the same power level, the TEM_{00} mode laser beam focuses energy at a smaller area, and the average intensity is higher in the irradiated region. Correspondingly, the aspect ratio of the TEM_{00} mode is much larger than the other three modes. From Fig. 13(c), it can also be noted that TEM_{00} mode takes a shorter time to reach a stable aspect ratio. Those properties determine that the TEM_{00} mode laser beam is a superior choice for welding, cutting and drilling. Although cylindrical TEM_{10} has the same peak intensity as TEM_{00} at the beam center, the central part only accounts for part of the energy. The average intensity of the total irradiated region is lower than the TEM_{00} mode, so that the melt pool is shallower than that of the TEM_{00} mode. Moreover, the rest of the energy is distributed in the ring band and causes the surface in the band region to melt at about $t = 2$ ms, which substantially enlarges the diameter of the melt pool. Meanwhile, the depth of the melt pool has a very small increment; thus, a drop of the aspect ratio value is observed in an early stage ($t < 4$ ms). For the cylindrical TEM^{*}_{01} mode, the laser beam has the lowest peak intensity such that the melt pool is relatively shallow until a vortex is formed. During this period, its aspect

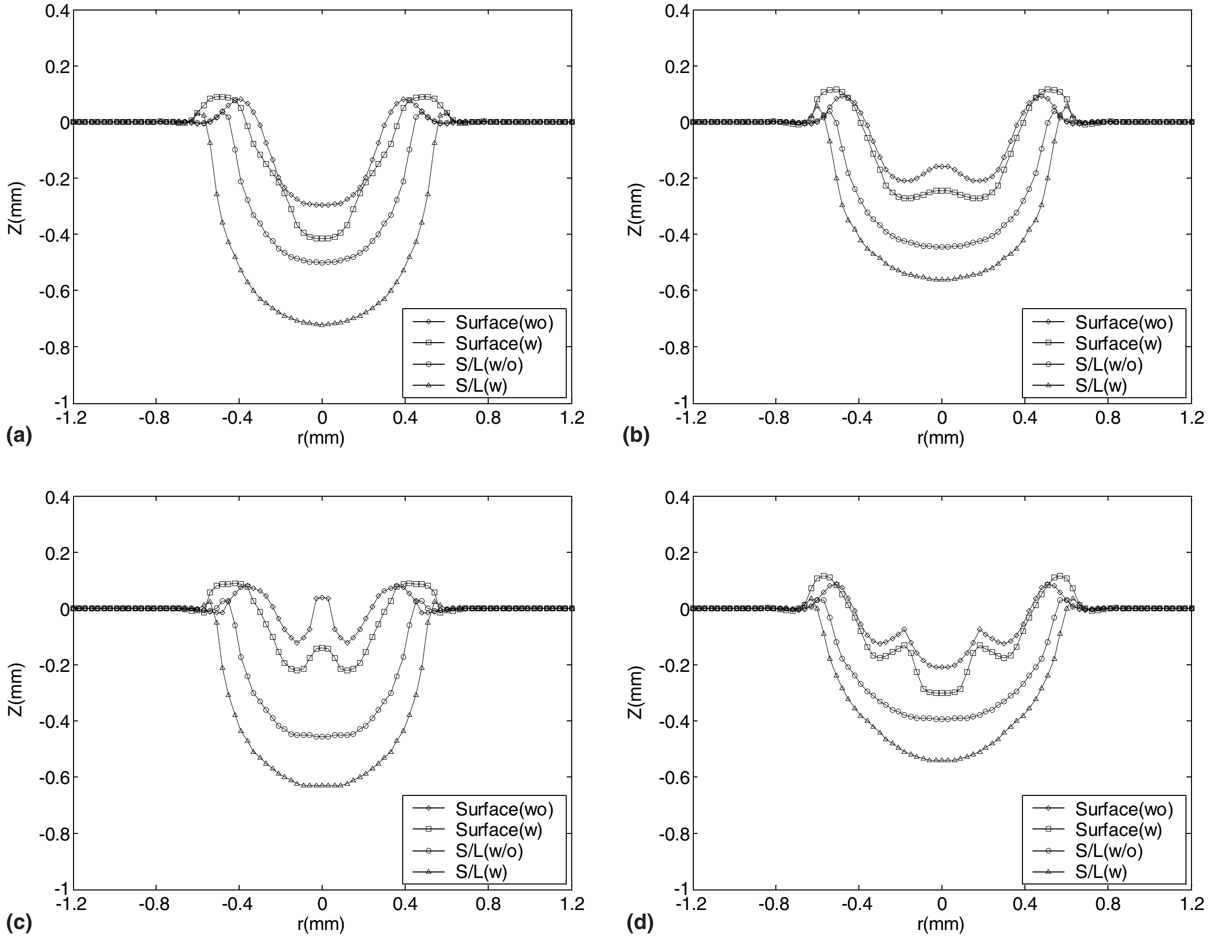

Fig. 12. Effect of recoil vapor pressure on melt pool shape. (a) TEM_{00} mode, (b) TEM_{01}, (c) TEM_{01}^{*}, and (d) TEM_{10}.

ratio is the smallest among those four beam modes. After 25 ms, the aspect ratio exceeds the cylindrical TEM_{10} mode due to a faster increment in the depth. Compared to the cylindrical TEM_{01}^{*} mode, the irradiated area of the rectangular TEM_{01} mode is around 50% smaller, and laser beam energy mainly distributes along the *y*-axis. Therefore, the diameter of the melt pool in the *y*-direction is larger than that of the cylindrical TEM_{01}^{*} mode, however, it is smaller in the *x*-direction.

5. Conclusion

The formation and evolution of the melt pool for four different types of laser modes are investigated based on a continuum model and level set algorithm. In this model, the surface shape of the melt pool, velocity field and temperature distribution are calculated. Different intensity profiles lead to distinct temperature distribution. Temperature gradient gives rise to the Marangoni shear stress, which is the primary driven force, and affects the velocity field. Flow pattern plays an apparent role in the surface temperature distribution and melt pool shape. From the simulation results, the following conclusions are achieved:

(1) The melt pool of the TEM_{00} mode has the greatest aspect ratio and develops quickly, which indicates that it is a superior mode option for cutting and drilling.
(2) Compared to the results of the TEM_{00} mode, the melt pool of the cylindrical TEM_{01}^{*} is wider but shallower. This feature shows that the cylindrical TEM_{01}^{*} mode may offer some advantages in a low intensity laser material process, such as cladding and surface alloy.
(3) In the melt pool evolution, the rectangular TEM_{01} mode has the similar features of two separate heat sources, and it could be the alternative for the dual beam in some situations.
(4) Melt pool formation of the cylindrical TEM_{10} mode possesses the combined features of TEM_{00} and cylindrical TEM_{01}^{*} mode. Flow pattern and isotherms in

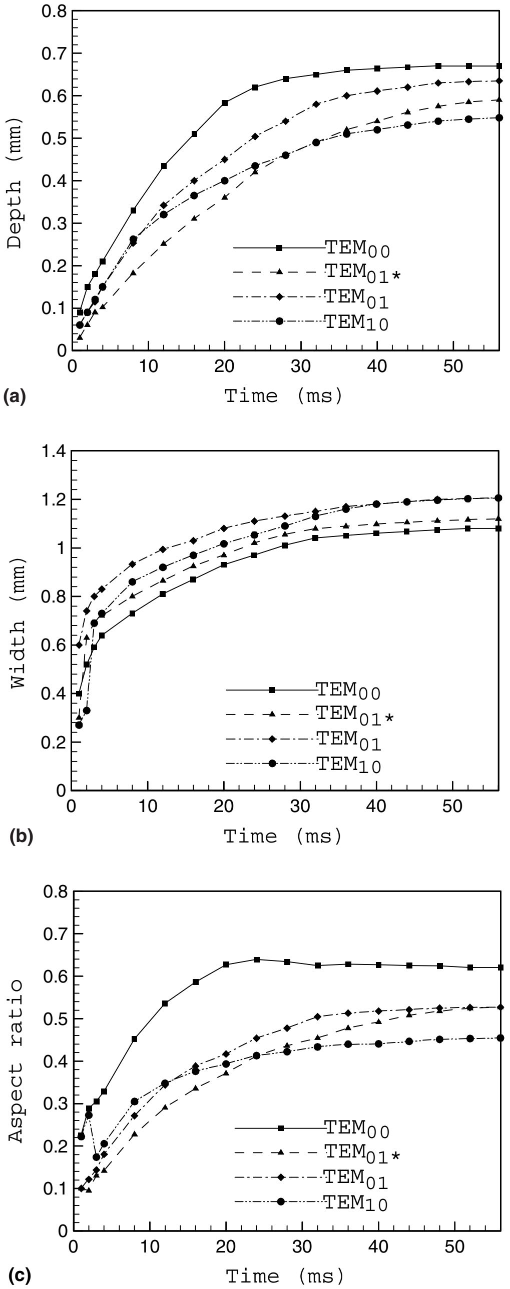

Fig. 13. Aspect ratio of the melt pool. (a) TEM_{00}, (b) TEM_{10}, (c) TEM_{01}^{*}, and (d) TEM_{01}.

the liquid region are more irregular than in the other three beam modes.

Acknowledgements

This research was supported by the National Science Foundation Grant Number DMI-9871185, the grants from the US Army Aviation and Missile Command (AMCOM) and US Air Force Research Laboratory contract # FA8650-04-C-5704. Their support is greatly appreciated.

References

[1] J. Mazumder, Overview of melt dynamics in laser processing, Opt. Eng. 30 (8) (1991) 1208–1219.

[2] A. Kaplan, G. Groboth, Process analysis of laser beam cladding, J. Manufact. Sci. Eng. 123 (2001) 609–613.

[3] C. Chan, J. Mazumder, M. Chen, A two-dimensional transient model for convection in laser melted pool, Metall. Mater. Trans. 15A (1984) 2175–2184.

[4] C. Chan, J. Mazumder, M. Chen, Effect of surface tension gradient driven convection in laser melt pool: three dimensional perturbation model, J. Appl. Phys. 64 (11) (1988) 6166–6174.

[5] F.R. Tsai, K.A. Elijah Jr., Modeling of conduction mode laser welding process for feedback control, J. Manufact. Sci. Eng. 122 (2002) 420–428.

[6] H. Ki, P.S. Mohanty, J. Mazumder, Modeling of laser keyhole welding: Part I. Mathematical modeling numerical methodology, role of recoil pressure, multiple reflections and free surface evolution, Metall. Mater. Trans. 33A (2002) 1817–1830.

[7] W.H. Zhang, H.L. Tsai, Pore formation and prevention in deep penetration pulsed laser welding, ICALEO, 2002, Section C.

[8] M. Bianco, C. Rivela, S. Talentino, On-line surface treatment feasibility of industrial components by means of CO_2 power laser, in: Proc. Laser Materials Processing: Industrial and Microelectronics Applications, SPIE, vol. 2207, pp. 53–61.

[9] D. Triantafyllidis, L. Li, F.H. Stott, The effect of beam shape in laser surface treatment of ceramics, ICALEO, 2002, Section B.

[10] W. Bennon, F. Incropera, A continuum model for momentum, heat and species transport in binary solid-liquid phase change systems—I. Model formulation, Int. J. Heat Mass Transfer 30 (10) (1987) 2161–2170.

[11] W. Bennon, F. Incropera, A continuum model for momentum heat and species transport in binary solid–liquid phase change systems—II, Int. J. Heat Mass Transfer 30 (10) (1987) 2171–2187.

[12] D.A. Knoll, D.B. Kothe, B. Lally, A new nonlinear solution method for phase change problems, Numer. Heat Transfer 35B (1999) 439–459.

[13] C. Prankash, V. Voller, On the numerical solution of continuum mixture model equations describing binary solid–liquid phase change, Numer. Heat Transfer 15B (1989) 171–189.

[14] B.D. Nichols, C.W. Hirt, R.S. Hotchkiss, SOLA-VOF: a solution algorithm for transient fluid flow with multiple free boundaries, LA-8355, Los Alamos National Laboratory, 1980.

[15] S.O. Unverdi, G. Tryggvason, A front-tracking method for viscous incompressible multi-fluid flows, J. Comp. Phys. 100 (25) (1992) 25–37.

[16] S. Osher, J.A. Sethian, Fronts propagating with curvature-dependent speed algorithms based on Hamilton–Jacobi formulations, J. Comp. Phys. 79 (1) (1988) 12–49.

[17] S. Popinet, S. Zaleski, A front-tracking algorithm for accurate representation of surface tension, Int. J. Numer. Meth. Fluids 30 (6) (1999) 775–793.

[18] D.B. Kothe, R.C. Mjolsness, M.D. Torrey, Ripple: a computer program for incompressible flows with free surfaces, LA-12007-MS, Los Alamos National Laboratory, 1991.

[19] J.U. Brackbill, D.B. Kothe, C. Zemach, A continuum method for modeling surface tension, J. Comp. Phys. 100 (1992) 335–353.

[20] Y. Wang, H.L. Tsai, Impingement of filler droplets and weld pool dynamics during gas metal arc welding process, Int. J. Heat Mass Transfer 44 (11) (2001) 2067–2080.

[21] S.V. Patankar, Numerical Heat Transfer and Fluid Flow, Hemisphere, New York, 1980.

[22] J.A. Sethian, Level Set Method and Fast Marching Methods, second ed., Cambridge University Press, Cambridge, UK, 1999.

[23] Y.C. Chang, T.Y. Hou, B. Merriman, S. Osher, A level set formulation of Eulerian interface capturing methods for incompressible fluid flows, J. Comp. Phys. 124 (1996) 449–464.

[24] M. Sussman, P. Smereka, S. Osher, A level set approach for computing solutions to incompressible two-phase flow, J. Comput. Phys. 114 (1) (1994) 146–159.

[25] G.P. Sasmal, J.I. Hochstein, Marangoni convection with a curved and deforming free surface in a cavity, J. Fluids Eng. 116 (1994) 577–582.

[26] V. Semak, A. Matsunawa, The role of recoil pressure in energy balance during laser materials processing, J. Phys. D: Appl. Phys. 30 (1997) 2541–2552.

[27] J.B. Bell, P. Colella, H.M. Glas, A second-order projection method for the incompressible Navier–Stokes equations, J. Comp. Phys. 85 (1989) 257–283.

[28] J.B. Bell, D.L. Marcus, A second-order projection method for variable-density flows, J. Comp. Phys. 101 (1992) 334–348.

[29] C.W. Shu, S.J. Osher, Efficient implementation of essentially non-oscillatory shock capturing schemes II, J. Comp. Phys. 83 (12) (1989) 32–78.

[30] M. Sussman, A. Almgren, J. Bell, P. Colella, L. Howell, M. Welcome, An adaptive level set approach for incompressible two-phase flows, J. Comp. Phys. 148 (1999) 81–124.

[31] M. Sussman, E. Fatemi, P. Smereka, S. Osher, An improved level set method for incompressible two-phase flows, Comput. Fluids 27 (5) (1998) 663–680.

[32] R. Scardovelli, S. Zaleski, Direct numerical simulation of free-surface and interfacial flow, Annu. Rev. Fluid Mech. 31 (1999) 567–603.

[33] Y. Wang, Q. Shi, H.L. Tsai, Modeling of the effects of surface-active elements on flow patterns and weld penetration, Metall. Mater. Trans. 32B (2001) 145–161.

[34] M.R. Boddu, S. Musti, R.G. Landers, S. Agarwal, F.W. Liou, Empirical modeling and vision based control for the laser metal deposition process, in: Twelfth Annual Solid Freeform Fabrication Symposium, Austin, Texas, August 6–8, 2001, pp. 452–459.